Alloys-By-Design: Application to titanium alloys for optimal superplasticity

E. Alabort[a], D. Barba[c], M.R. Shagiev[b], M.A. Murzinova[b], R.M. Galeyev[b], O.R. Valiakhmetov[b], A.F. Aletdinov[b], R.C. Reed[c]

[a] *OxMet Technologies Ltd., Unit 15, Oxford Industrial Park, OX5 1QU, United Kingdom*
[b] *Institute for Metals Superplasticity Problems, 39 Khalturin Str., Ufa 450001, Russia*
[c] *Department of Engineering Science, University of Oxford, Parks Road, Oxford, OX1 3PJ, United Kingdom*

Abstract

An alloy design approach for titanium alloys is presented. New alloys are isolated, manufactured and tested with an emphasis on the superplastic response. The superplastic effect is found to be optimal between 650 to 750°C at strain rates between 8.3×10^{-2} and 8.3×10^{-3}/s – this is a substantial improvement in terms of temperature and deformation rates over traditional titanium alloys such as Ti-6Al-4V. Elongations approaching ∼2000% are demonstrated. Electron backscatter diffraction studies confirm a randomisation of texture and absence of significant intragranular dislocation density, confirming superplasticity and thus grain-boundary sliding as the overarching deformation mechanism. At strain rates faster than 0.01/s, the alloys exhibit large elongations (∼200-500%) but softening is evident and lower ductility results. Our results reveal that the physical factors controlling the alloy composition/property/manufacturing interrelationship are understood and quantified. Physically-based constitutive equations are presented and used to demonstrate the practical advantages of the designed alloys.

Keywords: superplasticity, titanium alloys, constitutive modelling, superplastic forming, design

1. Introduction

Titanium alloys can be made to deform superplastically [1, 2, 3, 4]. Hence – provided they loading configurations are favourable – large elongations can be reached [5] which opens up possibilities for the fabrication of novel structures and components of complex geometry [6]. Usually, for this response to be triggered, the temperature must be in excess of 850-900°C; moreover, the strain rate (either imposed or induced) must not exceed 10^{-3}/s. The Ti-6Al-4V alloy or its variants are most commonly employed for superplastic applications. There are significant applications in the aeronautics, space, transportation and biomedical sectors.

Nevertheless, one can argue that titanium alloys which exhibit this superplastic behaviour could be more widely employed. One barrier is the high processing temperature needed, which confers (i) excessively high energy costs but also (ii) excessive tool wear/failure necessitating its frequent replacement, and (iii) need for protective atmosphere to prevent oxidation. A further concern is the relatively low strain rates needed which translates into rather low rates of component production; if these could be increased, this would be beneficial in terms of manufacturing efficiency. A very credible way to deal with these challenges is to design new grades of titanium alloys which are more amenable to processing, either by lowering the temperature needed for the superplastic effect to be induced or else by allowing for a greater strain rate to be effective.

The research here was carried out with the above in mind. In recent years, there has been a significant improvement in our understanding of physical basis of the superplastic effect, which has arisen for example *via* careful high temperature experiments [7] and theoretical analysis [8, 9]. The role of the two phase (α/β) structure in inducing stable superplasticity without grain growth has become evident; this insight can be exploited. This led us to believe that it might be possible to isolate new, improved compositions of titanium alloy for such applications based upon so-called alloys-by-design routes based upon high-throughput calculations. Such design work was carried out prior to experimental testing reported here.

2. Background

The formability of titanium alloys is enhanced by three factors: (i) fine grain sizes [10], (ii) high temperatures [11], or (iii) low strain rates [12]. Unfortunately, these make the processing and manufacture of components expensive and inefficient. How can one overcome these? First, one may revisit the mechanisms of grain boundary sliding in titanium and its alloys [13]. The mechanisms of superplastic deformation in titanium alloys seems to be well known [14, 15, 16, 17]. Most of the accommodation is carried out by the β phase – it has more slip systems active and higher diffusivity than α. Therefore, more β phase must be desirable. However, with high volume fractions of β, rapid grain growth occurs [18], grain elongation is more likely, and boundary sliding is less dominant. If the volume fraction of β is too low, the accommodation requires α to deform [19]. Due to lower diffusivity and less favourable slip activity, high forming stresses result – cavitation impedes optimal formability and dynamic recrystallisation induces inhomogeneous flow [4]. An optimal α/β balance exists [17].

This limitations can be short-came with ultra-fined grained microstructures – with sizes below 1μm even fully α microstructures can exhibit superplasticity at low temperatures [20]. For example, ultra-fine grained Ti-6Al-4V can achieve excellent elongation at temperatures as low as 600°C [21]. However, this requires processing *via* severe plastic deformation techniques [22] – *e.g.* high pressure torsion and equal-channel angular pressure. Unfortunately, these methods increase the material processing cost. Moreover, the amount of material which can be processed by these methods is limited. Because of this, we focus on reformulating the alloy chemistry to induce optimal formability rather than proposing novel processing techniques. This paper proposes novel alloys with optimal formability by; (i) introducing more β-stabilisers to obtain an optimal phase ratio at low temperatures; and (ii) by increasing the effective diffusivity to facilitate accommodation – see Figure 1.

Traditionally, new alloys have been designed through empiricism – their chemical compositions have been isolated using time consuming and expensive

experimental campaigns. The large number of possible alloying elements indicates that these alloys are not entirely optimised and that alloys with more desirable properties are likely to exist. Alternatively, the CALPHAD method (CALculate PHAse Diagram) can be used to calculate the phase diagram and thermodynamic properties for a large series of alloy compositions. Then, this information can be used to make estimates of the relevant thermo-mechanical properties across a very broad compositional space. This is the alloys-by-design method. Such modelling strategy is adopted here, and it is used to isolate new grades of titanium alloys with the most optimal formability.

With the above in mind, this paper explores the alloys-by-design method in titanium alloys. First, the design framework is presented: this is used to define an optimal alloy space. Second, three alloy examples are produced for validation. Third, the alloys are tested to prove optimal formability. Fourth, the mechanical performance of the designed alloys is measured and compared to Ti-6Al-4V. Finally, a constitutive model that captures the behaviour of the alloys is proposed. This is used to simulate a formability benchmark experiment to highlight the potential advantages of the developed alloys.

3. Modelling methods for alloy design

The first step in the design process is the definition of an elemental list along with the associated upper and lower compositional limits. The second step employs thermodynamic calculations to estimate the fraction of each phase at equilibrium and their associated compositions. During a third step, a series of properties to optimise for – here called merit indeces – are proposed. These will be used to isolate and rank the most optimal alloys. The following merit indeces are defined:

- **Temperature for optimal superplasticity:** *i.e* the temperature where the microstructure is composed by approximately 40% β-phase and 60% α-phase. Equilibrium thermodynamic calculations are carried out to determine this temperature for each composition. This was defined following

Table 1: Diffusivity (D) of β-stabilising elements at 870°C.

Element	Ni	Co	Fe	Cr	β-Ti	V	Nb	Al	Mo	W
D(cm^2s)$\times 10^{-10}$	220	190	78	11	3.36	2.4	1.7	1.4	0.6	0.2
$D_{\text{element}}/D_{\beta-\text{Ti}}$	63.7	55.3	22.6	3.2	1	0.69	0.49	0.43	0.17	0.06

$$T_{\text{SPF}} = \begin{cases} T(\Phi_{\beta/\alpha\rightarrow 0.4}) & T_{\text{SPF}}/T_m \geq 0.4 \\ - & T_{\text{SPF}}/T_m < 0.4 \end{cases} \tag{1}$$

where $T(\Phi_{\beta/\alpha\rightarrow 0.4})$ is the temperature of 40%β and T_m is the melting point of the alloy. If $T_{\text{SPF}}/T_m < 0.4$, the thermally activated mechanisms of deformation are impeded and the composition is discarded.

- **Diffusivity of β-phase:** faster diffusivities translate into a lower forming stress. This can be achieved by adding small amounts of elements with high tracer diffusivities – *e.g.* Fe, Ni and Cr. Here, it is considered that the diffusivity is controlled by the faster diffusing species consistent with

$$D_\beta = \sum_i x_{\beta,i} D_i \tag{2}$$

where $x_{\beta,i}$ is the atomic fraction of the ith element in the β phase, and D_i is its tracer diffusivity as given in [23] and summarised in Table 1.

- **Density:** this is calculated using a simple rule of mixtures and applying a correctional factor of 5% following

$$\rho = 1.05 \sum_i x_i \rho_i \tag{3}$$

where ρ_i is the density for a given element and x_i is the atomic fraction of the alloy element.

- **Raw elemental cost:** as with density, a simple rule of mixtures is considered following

$$\text{Cost} = \sum_i w_i c_i \tag{4}$$

where c_i is the cost of the ith element, and w_i is its weight fraction. Our estimates assume that processing costs are identical for all alloys, *i.e.* that the product yield is not affected by composition.

- **Microstructural stability:** this relates to the susceptibility of the alloy to avoid the precipitation of brittle intermetallic phases. This is calculated in terms of Fe-Cr-Ni equivalent weight fraction. It is established that the following relationship

$$\mathrm{Fe} + \mathrm{Ni} + \mathrm{Cr} \leq 3.0\mathrm{wt.\%} \tag{5}$$

needs to be satisfied to avoid brittle intermetallic – their formation would translate into a loss of ductility.

- **Machinability:** aluminium content is related directly to both the strength and the machinability of the alloy. High values (>7 wt.%) of aluminium will cause a brittle behaviour by creating intermetallic particles. Medium aluminium content (3-6 wt. %) provides good strength but machinability is still difficult. No aluminium content facilitates greatly the cold machinability and improves ductility at expense of the strength. This led to define the following maximum aluminium content restriction:

$$\mathrm{Al} < 2.5\mathrm{wt.\%}. \tag{6}$$

- **Strength:** this is calculated following [24]

$$\sigma = 60[\mathrm{Al}]^{\sigma}_{\mathrm{eq.}} + 50[\mathrm{Mo}]^{\sigma}_{\mathrm{eq.}} + 235 \tag{7}$$

where $[\mathrm{Al}]^{\sigma}_{\mathrm{eq.}}$ and $[\mathrm{Mo}]^{\sigma}_{\mathrm{eq.}}$ are the aluminium and molybdenum strength equivalent defined following

$$\begin{aligned} [\mathrm{Al}]^{\sigma}_{\mathrm{eq.}} &= \mathrm{Al} + \mathrm{Zr}/3 + \mathrm{Sn}/6 + 3.3\mathrm{Si} + 20\mathrm{O} + 33\mathrm{N} \\ [\mathrm{Mo}]^{\sigma}_{\mathrm{eq.}} &= \mathrm{Mo} + 0.6\mathrm{V} + 1.25\mathrm{Cr} + 1.42\mathrm{Fe} + \mathrm{Ni} \end{aligned} \tag{8}$$

where all the elemental quantities are in weight %.

In the fourth stage, design constraints are introduced. These will isolate the optimal alloy space. The final stage involves the analysis of the optimal dataset which remains to find particular alloy compositions.

4. Experimental methods

In this section, the methods used to produce the novel alloys and the methods employed to measure their properties are described.

4.1. Material processing

Trial ingots of the novel titanium alloys weighting 100 g were produced using a laboratory argon arc melting machine. Titanium sponge TG90 and chemically pure aluminium, vanadium, iron, nickel, molybdenum, silicon and boron were used as starting materials. The alloys were repeatedly remelted by argon-arc method to increase the homogeneity of the alloying elements. After casting, the alloys were thermo-mechanically processed employing multi-step isothermal forging and sheet-rolling to obtain a fine equiaxed microstructure. Temperature conditions for the processing were defined as a function of the β-transus temperature for each alloy. Those were measured using differential scanning calorimetry (DSC). DSC is also to compare the actual β-transus temperature to the predictions provided by the thermodynamic calculations. The chemical composition and microstructure of the alloys were examined using a Tescan Mira 3LMH scanning electron microscope equipped with an X-ray energy dispersive spectrometer (EDS). The analysis was performed in at least six points uniformly distributed within the polished section of the ingot.

4.2. High temperature tensile testing

Superplasticity in the titanium alloy was evaluated using specimens measuring 10 mm in gauge length, 4 mm in width and 0.8 mm in thickness. These were extracted from the sheet using electro-discharge machining and then polished to ensure appropriate surface finish. Isothermal, constant displacement-rate tensile tests were carried out using an Instron 5982 electro-mechanical testing

machine. Temperatures ranged from 550 to 800 °C at 50 °C intervals between tests. Initial strain rates of 1.7×10^{-2}, 8.3×10^{-3}, 1.7×10^{-3} and 8.3×10^{-4} /s were applied. At 750 °C, specimens were also tested at an initial strain rate 8.3×10^{-2}. Tests were performed in air and the deformation was held until rupture.

4.3. Room temperature tensile and fatigue testing

For room temperature properties, samples measuring 40 mm in length, 3 mm in width and 1 mm in thickness with reduced gauge length measuring 8×1.5×1 mm were machined using electro discharge machining from the sheet blanks. The samples were then plane polished to remove any damage from the surfaces. For testing, an electro-pulse testing machine was employed. Tensile tests were carried out at a strain rate of 0.01/s. Digital image correlation was used for strain measurement – the surface of the sample was speckled and the ends of the gauge section where used to monitor deformation. Fatigue tests where carried out at a frequency of 45 Hz with a stress ratio of R=0.1. Cycling was maintained until failure or until 10 million cycles where reached.

5. Results and discussion

In this section, first the rational around the design of the novel compositions is described. This is used to isolate a series of example compositions that are then subjected to experimentation to measure their superplastic properties and their room temperature mechanical performance.

5.1. Design optimisation for low-temperature superplasticity

Three new superplastic titanium alloys are now isolated. The intention is to design a family of alloys that allow unprecedented levels of efficiency and cost reduction in the industrial exploitation of superplasticity. The aim is to achieve a combination of good service properties, improved superplastic formability, and lower material cost. Within those properties, the alloy space should offer

Alloying element		Al	V	Fe	Ni	Mo	Si	B	O	Ti
Alloy 1	Target	0.75	0.5	2.75	0.25	1.0	0.0	0.05	<0.2	Bal.
	Mean content	0.73	0.49	2.84	0.27	0.99	0.0	n/a	n/a	Bal.
Alloy 2	Target	1.5	1.5	2.75	0.25	3.0	0.0	0.1	<0.2	Bal.
	Mean content	1.59	1.58	2.72	0.31	3.11	0.0	n/a	n/a	Bal.
Alloy 3	Target	2.25	1.5	0.25	2.75	2.0	0.15	0.1	<0.2	Bal.
	Mean content	2.28	1.48	0.30	2.86	2.11	0.2	n/a	n/a	Bal.

Table 2: Chemistry of the designed alloys.

improved performance than current grades of superplastic alloys, namely the Ti-6Al-4V, ATI425, Ti54M, and SP700 – baseline alloys from now on. Figure 1(a) shows the trade-off between the SPF temperature and the raw material cost. An optimal region is defined – this area has lower SPF temperature and lower elemental cost than the baseline alloys. Figure 1(b) shows the trade-off between SPF temperature and density – due to the reduction in Al, the density of the optimal alloy space will necessarily be higher than baseline alloys. A maximum density of $1.05\rho_{\text{Ti-6Al-4V}}$ was defined. Figure 1(c) shows the trade-off between the SPF temperature and the normalised diffusivity. Fast diffusing elements such as Fe and Ni are added witihin reasonable quantities to increase diffusivity while avoiding the formation of brittle intermetallic phases. Figure 1(d) illustrates the trade-off between predicted strength, superplastic temperature and aluminium content.

Within the optimal space that Figure 1 highlights, three alloy examples are proposed: (i) Alloy 1 – optimised for low elemental cost; (ii) Alloy 2 – optimised for low SPF temperature; and (iii) Alloy 3 – optimised for high diffusivity. The chemistries of each one of the proposed alloys are provided in Table 2. The table highlights the nominal compositions and the mean measured values.

Electron-backscattered diffraction (EBSD) inverse pole figure maps of the sheet surface and sheet cross-section taken after the last rolling step are presented in Figure 2. Both the α and the β phases are shown – the alloys have around 15 to 30% β phase present at room temperature. The linear interception

method was used on the sheet-surface micrographs to determine the mean grain size of each alloy – these are plotted as frequency-grain diameter diagrams in the bottom part of Figure 2. Both α and β grains were measured. The alloys have a mean grain size between 2.2 and 3.1 μm. SEM-BSE images of the final microstructures are also provided in Figure 2.

Figure 3 shows the differential scanning calorimetry results – it reveals that Alloys 1 and 3 have a β-transus temperature of 850 and 855°C respectively. On the other hand, Alloy 2 has a slightly lower temperature 832°C – see Fig. 3(b). Thermodynamic calculations predict β-transus temperatures of 812, 792, and 825°C for Alloys 1, 2, and 3 respectively. Comparison shows a difference of 35, 38 and 30°C between prediction and measurement for each of the alloys. Although there is a slight difference between model and experiment, the relative β stability of the alloys is captured well. This difference may be also due to some shift of the experimental curve during continuous heating, or to the presence of O, C, N in the experimental alloys.

Following, the properties of the designed alloys are measured to prove the designed performance. Figure 4 illustrates the measured stress - strain response at different temperatures and strain rates. Figure 4(a) shows the mechanical response at temperatures between 600 and 800°C at a strain rate of 8.3×10^{-4}/s. Rheological analysis indicates that formability is optimal between 700 and 750°C: the stresses are low, hardening is limited, total elongation is very high, and no flow softening is appreciated. Figure 4(b) shows the effect of strain rates at those optimal temperatures. As the strain rate increases, the forming stress increases and total elongation decreases. Figure 4 illustrates the tested samples of each alloy after deformation at 8.3×10^{-4}/s.

5.2. On the effect of strain rate on superplasticity

The value of total elongation is considered a good indicator of the formability – values in excess of 300-400% indicate that the superplastic effect is strong. Figure 5(a-b) shows the values of total elongation as a function of the strain rate for temperatures of: (a) 700°C and (b) 750°C. Alloys 2 and 3 show su-

perplastic elongations at strain rates as fast as 1×10^{-2}/s at 750°C. The alloys show elongations in excess of 1500% at strain rates of $\sim1\times10^{-3}$. At 700°C, the effect is considered strong at strain rates of $\sim5\times10^{-3}$/s and below.

The strain rate sensitivity coefficient m is equally important. A high value of m means that the material is less prone to necking and inhomogeneous straining, therefore improving formability. The strain rate sensitivity parameter m is measured *via* the logarithmic relationship between the stress σ and the strain rate $\dot{\varepsilon}$ for a given value of strain ε and temperature T. This is calculated following $m = \frac{\partial \ln \sigma}{\partial \ln \dot{\varepsilon}}\big|_{\varepsilon,T}$. Figure 5 shows the derived values of m at (c) 700°C and (d) 750°C at a strain of 0.1. Values of m larger than 0.5 are reported at 750°C – these indicate excellent formability. At 700°C, high m values are also reported ($\sim$0.4) – these still provide excellent deformation stability. Figure 5(c-d) also shows that an increasing testing temperature allows for higher m values at higher strain rates.

5.3. On the effect of temperature on superplasticity

Figure 6(a-b) shows the dependence of the flow stress at 0.1 strain with temperature. The flow stress tends to decrease with increasing temperature up to a threshold – between 750 and 800°C – when the flow stress increases again. This is probably due to rapid grain growth and to a high volume fraction of β-phase which impedes grain boundary sliding. Alloy 2 (the most β-stabilised one) shows the strongest increase in flow stress. Figure 6(a-b) also shows that Alloy 3 has the lowest flow stress at 800°C – this is also consistent with the design intent presented in Figure 1 (high diffusivity). When comparing to the baseline alloys [25], the proposed alloys can be formed under lower stresses, faster rates and lower temperatures.

Figure 6(c) shows the total elongation as a function of the temperature. It is evident that the most optimal regime is within 700 and 750°C. Moreover, Alloy 2 exhibits superplastic elongation at temperatures as low as 600°C. Indeed, Alloy 2 exhibits optimal superplasticity at lower temperatures than Alloys 1 and 3 – this is consistent with the design intent presented in Figure 1.

The data presented in Figure 6(a) is then used to calculate the apparent activation energy Q as given by the slope of the data when plotted as $\frac{1}{RT}$ vs $\ln\left(\frac{\dot{\varepsilon}^m}{\sigma}\right)$. Figure 6(d) shows the logarithmic value of stress against the inverse of the temperature. When assuming a value of $m = 0.5$, the apparent activation energy Q can be estimated directly. The data shows a shift in slope between low and mid temperatures. The first region corresponds to T=550-600°C where no superplasticity was observed. The second region: T=650-750°C correspond to low-temperature superplasticity. At the highest temperature, the stress values do not follow the identified trend. This is believed to be caused by substantial changes occurring at the microstructural level – grain growth in particular. The dependence presented in Figure 6(d) can also be used to introduce the dependence of the temperature in a constitutive model – this will be discussed in the following section.

5.4. Effect of deformation on microstructure

SEM-BSE images of the samples after deformation are used to elucidate the micromechanisms of deformation in these alloys. The analysis is carried out in Alloy 2, but similar results are expected in the other 2 alloys. Figure 7 shows the microstructure at different strain points – taken at different points across the sample length. The local strain is estimated following $\varepsilon = \ln(A_0/A)$ where ε is the local strain, A_0 is the initial cross-sectional area, and A is the area where the scan was taken. Figure 7(a) shows micrographs for a strain rate of 8.3×10^{-4}/s and different temperatures while Figure 7(b) shows micrographs for a temperature of 750°C and different strain rates.

Microstructural characterisation is now used to elucidate the particular micromechanisms of deformation. The following details are observed; (i) at temperatures above 750°C, grain growth – both static and dynamic – is evident. The mean grain size increases substantially. This is reflected as hardening in the stress-strain curves shown in Figure 4; (ii) as the strain rate increases, grain growth is less severe – static grain growth is less likely due to reduced exposure time. Dynamic recrystallisation may also be present at higher strain rates.

Moreover, under fast strain rates and high levels of strain, grains tend to elongate along the tensile direction. This behaviour evidences low superplasticity and ductility; and (iii) as the temperature decreases, the microstructure stabilises, the equiaxiality is maintained, and the optimal phase ratio is observed – these conditions are optimal for high ductility. As the temperature keeps decreasing (lower than 650°C), the diffusion activity is too low – high flow stress and lower ductility result.

Figure 7(c) shows EBSD scans of Alloy 2 before and after deformation at 750°C an a strain rate of 8.3×10^{-4}/s. Analysis indicates a randomisation of the texture even at high strains. This evidences that grain boundary sliding is the primary deformation mechanism.

5.5. Room temperature mechanical properties

The mechanical properties of the new alloys at room temperature were evaluated. The alloys were tested under tension at a strain rate of 0.01/s until failure for both longitudinal and transverse rolling directions. The same experimentation was carried out for the titanium alloy Ti-6Al-4V with a mean grain size of $\sim 6\mu$m [19]. The stress - strain response of the alloys is shown in Figure 8(a) while fatigue is shown in Figure 8(b). As predicted, the strength of the new alloys is lower than Ti–6Al-4V, but an increase in the total elongation is reported. One should also note that as a consequence of adding large amounts of strong β stabilisers and fast diffusers, the creep resistance or temperature of operation of the new alloys will be lower than the benchmark alloy Ti-6Al-4V.

Figure 8(c-f) summarises and compares the values of yield strength, the ultimate tensile strength (UTS), the ductility, and the dissipated energy. The new alloys have a lower strength but higher ductility and dissipated energy than Ti-6Al-4V. Figure 8(c) compares the modelled and the measured strength – these are in good agreement. The reduction in strength is due to lower aluminium and oxygen content – oxygen was not treated as an alloying element in this work. Despite the decrease in strength, an improvement in ductility and dissipated energy can provide advantages in engineering applications where high

toughness is important. Moreover, lower strength and improved ductility could facilitate machining.

Figure 8(b) compares the fatigue performance of the new alloys with Ti-6Al-4V. Fatigue tests were carried out at 700, 600, 500, 400 and 300 MPa. Curves comparing the stress amplitude against the cycles to failure show that there is an offset of approximately 100 MPa between Alloys 2-3, and Ti-6Al-4V. This means that under the same fatigue life target, Ti-6Al-4V is able to withstand an additional 100 MPa. These results are consistent with the measurements of static strength presented in Figures 8. Reported values of fatigue strength for Ti-6Al-4V alloy are slightly lower than those reported in the literature when similarly processed [26]. Typically, Ti-6Al-4V shows a ratio of fatigue strength to yield strength of approximately 0.6. However, our experiments show a ratio of ≈ 0.5. This difference may be due to the size of the tested specimen – the miniaturised specimens had a high surface to volume ratio; any imperfection present will have a stronger impact than in large-scale fatigue samples. Nevertheless, the purpose of the experimentation is comparative – the trends observed in tensile testing are also observed under fatigue and those are useful to understand the limitations of the new alloys against the benchmark Ti-6Al-4V.

6. Application: modelling of superplastic forming

In this section, the measured flow stress data is used to calibrate a microstructural sensitive model that captures the effect of grain size and volume fraction of β phase on the superplastic properties of the alloys. Finally, the model is used to simulate a superplastic forming process and the results are used to illustrate the advantages of the developed alloy over Ti-6Al-4V.

6.1. Material model

To perform accurate simulations of forming processes, the behaviour of the material needs to be modelled. For this purpose, a unified vicoplastic constitutive model that considers dynamic changes in the microstructure and that

embeds the effect of different chemistries is introduced. This builds on the work developed by many [27, 28, 29, 30, 31, 32, 33]. The physical base of the model is described in detail in previous work from the authors [4, 19]. One of the most important characteristic of the model is the relationship between the stress, the strain rate, and the temperature. This can be expressed following

$$\dot{\varepsilon}_{\mathrm{p}} = (1 - f_\beta)\frac{D_\alpha}{d^p}\exp\left\{\frac{-Q_\alpha}{RT}\right\}\left(\frac{\sigma - \sigma_{\mathrm{b}}}{\sigma_0}\right)^{n_\alpha} + f_\beta\frac{D_\beta}{d^p}\exp\left\{\frac{-Q_\beta}{RT}\right\}\left(\frac{\sigma - \sigma_{\mathrm{b}}}{\sigma_0}\right)^{n_\beta} \tag{9}$$

where $\dot{\varepsilon}_{\mathrm{p}}$ is the steady state strain rate, f_β is the volume fraction of β phase, $D_{\alpha,\beta}$ is the diffusivity of the α and the β phase respectively, $Q_{\alpha,\beta}$ is the apparent activation energy of the deformation in the α and β phases respectively, d is the mean grain size – homogeneously treated across phases, p is the grain size exponent, $n_{\alpha,\beta}$ is the stress exponent, R is the gas constant, T is the temperature, σ_0 is the reference stress, and σ_{b} is the back stress defined following

$$\dot{\sigma_{\mathrm{b}}} = H\dot{\varepsilon}_{\mathrm{p}} - R_{\mathrm{d}}\dot{\varepsilon}_{\mathrm{p}}\sigma_{\mathrm{b}} \tag{10}$$

where H and R_{d} are material parameters.

This steady-state strain rate equation is a function of the mean grain size of the material. This will make the stress-strain path of the model sensitive to changes in the microstructure. The rate of change of the mean grain size can be divided in static and dynamic growth following

$$\dot{d} = \dot{d}_{\mathrm{static}} + \dot{d}_{\mathrm{dynamic}} \tag{11}$$

where the static grain growth process is modelled as an atomic diffusion phenomenon affected by temperature following [34]

$$\dot{d}_{\mathrm{static}} = \alpha_1\exp\left\{\frac{-Q_{\mathrm{st}}}{RT}\right\}d^{-\gamma_1} \tag{12}$$

where α_1 and γ_1 are material constants, and Q_{st} is the activation energy of the static growth process. Dynamic grain growth is modelled following [27]

$$\dot{d}_{\mathrm{dynamic}} = \alpha_2\exp\left\{\frac{-Q_{\mathrm{dn}}}{RT}\right\}\dot{\varepsilon_p}d^{-\gamma_2} \tag{13}$$

Table 3: β-phase volume fraction material parameters.

	a	b	c	d
	$[°C^{-3}]$	$[°C^{-2}]$	$[°C^{-1}]$	[-]
Alloy 1	5.86×10^{-8}	-1.13×10^{-4}	0.07303	-15.69
Alloy 2	4.26×10^{-8}	-7.91×10^{-5}	0.05012	-10.47
Alloy 3	7.5×10^{-8}	-1.42×10^{-4}	0.09051	-19.172

where α_2, γ_2 are material constants, and Q_{dn} is the activation energy of the dynamic grain growth process. Both of these will capture the observed grain growth and will translate into hardening at the rheological level.

6.1.1. Calibration of model parameters

Before the presented model can be employed, the material parameters need to be calibrated [35, 36]. First, because the strain rate is a direct function of the volume fraction of phases, the temperature dependence of the β volume fraction of each alloy needs to be determined. For this, an empirical relationship is defined following

$$f_\beta = aT^3 + bT^2 + cT + d \tag{14}$$

where a, b, c and d are fitting constants, and T is the temperature in Celsius. Parameters were calibrated to the phase fraction-temperature curve predicted *via* ThermoCalc after shifting the temperature by the difference between ThermoCalc and DSC measurements. The parameters of each alloy are listed in Table 3. This relationship is usable between 600 and β-transus temperature – *i.e.* when f_β reaches a value of 1. Figure 9 compares the model to experimental measurements extracted from Figure 7. Experiments and models are in good agreement.

Second, the steady-state relationship between stress, strain-rate and temperature is calibrated. Stress-strain values at strain values of 0.1 and below are used to calibrate the back stress parameters. These are used to capture the initial hardening which is caused by initial dislocation pile-up. The diffusivity parameters $D_{\alpha,\beta}$ are also calibrated, however, these are multiplied by the

Table 4: Material model parameters.

D_α (μm/s)	D_β (μm/s)	Q_α (J/mol)	Q_β (J/mol)	n_α (-)	n_β (-)
550	620	228131	207490	3.2	1
p (-)	σ_0 (MPa)	H (MPa)	R_d (-)	α_1 (-)	α_2 (-)
2	1	55	5.2	450	1×10^9
	γ_1 (-)	γ_2 (-)	Q_st (J/mol)	Q_dn (J/mol)	
	0.75	4.95	105000	152000	

normalised diffusivity parameters of each alloy given in Figure 1. Calibrated parameters are listed in Table 4.

Third, the grain size evolution parameters are calibrated. For this, the whole experimental stress-strain curve is used. An objective function optimises the parameters by comparing experimental and computed model curves. This approach assumes that hardening is due to an increase in the mean grain size exclusively. These parameters are also listed in Table 4.

The calibrated model is compared to the experimental stress-strain curves in Figure 10. The constitutive equations capture the dependence of the strain-rate and the temperature, but also the effect introduced by the chemistry – by including the effective diffusivity and the temperature-dependent β volume fraction. Figure 11 compares the computed grain size – extracted from the strain hardening – and the experimental measurements – shown in Figure 7. The calibrated behaviour is in good agreement with measurements. This validating the hypothesis that rheological changes in the strain path are caused by microstructural changes exclusively.

6.1.2. Cone formability simulation

To illustrate the advantages of the designed alloys, the material model is implemented into the finite element analysis (FEA) solver Abaqus standard and it is used to simulate a cone formability experiment. The described material model is implemented into FEA using a 'CREEP' subroutine as described in [37]. For discretisation, axisymmetric 2D elements (CAX4) are used. The cone

die is modelled using rigid elements. The metal sheet is clamped into place and a constant pressure of 1 bar is applied over a period of time of 1000 s. The simulated setup is illustrated in Figure 12(a). The simulations are used to evaluate the % of completion within that time span – where 100% represents the sheet reaching the bottom of the die. This experiment is used to assess the suitability of a material for superplastic forming and can be used to rank alloys based on their forming amenability. Alloys with optimal formability tend to form deeper and have homogeneous thinning – these depend on the flow stress and the strain rate sensitivity parameter m respectively.

In order to illustrate the advantages of the new alloy over the conventional Ti-6Al-4V alloy, the same experiment was simulated using the mechanical properties of Ti-6Al-4V. The constitutive model and the material parameters are described in Alabort *et al.* [19]. The model parameters were calibrated for a $\approx 6\mu$m mean grain size microstructure at temperatures between 750 and 900°C.

Figure 12(b) shows the geometry of each cone after the pressure is halted: first column when forming at 700°C and second column when forming at 750°C. The contour colours illustrate the distribution of creep equivalent plastic strain. One can observe that the strain distribution is rather uniform and necking is minimal. This is due to the high strain rate sensitivity of the alloys – these produce components of uniform thickness and reduced chances of cracking. One of the main challenges in the SPF industry is to increase the efficiency of production. The goal is to minimise the forming time while achieving successful formability. Figure 12(c) shows the completion percentage for each alloy and their advantages over conventional Ti-6Al-4V. This is an indicative of the speed of the process and highlights the importance of including fast diffusing elements reduce manufacturing time. Figure 12(c) also highlights the advantages of the developed alloys when superplastically forming at low temperatures.

7. Conclusions

The following conclusions can be drawn from this work:

1. A method to design titanium alloys with optimal formability is presented. The framework is used to design three prototype alloys that exhibit the superplastic effect at low temperatures and fast strain rates.
2. It is proven that the models are accurate enough to allow the regime of superplasticity to be pinpointed in a right-first-time fashion. The strain rate sensitivity parameter and the elongation to failure indicate optimal formability in the range of 650 to 750°C at strain rates between 10^{-2} and 10^{-3}/s, thus offering substantial improvement over legacy alloys.
3. Under the most optimal regime (750°C) elongations in excess of 1900% are achieved. More importantly, superplastic elongations – *i.e.* in excess of 400% – at temperatures as low as 600°C and strain rates as fast as 10^{-2} are reported.
4. The microstructure remains mostly equiaxed after large strains, thus confirming the superplastic effect. This, coupled with a randomisation of the crystallographic texture, indicates that grain boundary sliding is the main deformation contributor – even at such low temperatures. Grain growth is also reported at temperatures above 750°C, possibly promoted by the high diffusivity and volume fraction of β of the new alloys.
5. Room temperature properties indicate a reduction in strength and fatigue properties of approximately 100 MPa inferior to Ti-6Al-4V. However, the designed alloys offer improved ductility and dissipated energy, therefore making them suitable candidates for applications where impact toughness is important.
6. A constitutive model that embeds the temperature, microstructure, and strain-rate dependence of the alloys is proposed and calibrated. Simulations of cone formability experiments are used to visualise the difference in behaviour of each one of the alloys and to highlight their advantages in an industrial environment.

Acknowledgements

The authors are grateful to OxMet Technologies Ltd for funding this research. Part of the experimental work was performed using the facilities of shared services center 'Structural and Physical-Mechanical Studies of Materials' within the state assignment of the Institute for Metals and Superplasticity Problems.

References

[1] O. A. Kaibyshev, Superplasticity of Alloys, Intermetallides and Ceramics, Intermetallics and Ceramics (1992).

[2] T. G. Nieh, J. Wadsworth, O. D. Sherby, Superplasticity in metals and ceramics, University of Cambridge, 1997.

[3] S. L. Semiatin, V. Seetharaman, I. Weiss, Hot workability of titanium and titanium aluminide alloysan overview, Materials Science and Engineering: A 243 (1998) 1–24.

[4] E. Alabort, D. Putman, R. Reed, Superplasticity in Ti-6Al-4V: Characterisation, modelling and applications, Acta Materialia 95 (2015) 428–442.

[5] S. L. Semiatin, P. N. Fagin, J. F. Betten, A. P. Zane, A. K. Ghosh, G. A. Sargent, Plastic flow and microstructure evolution during low-temperature superplasticity of ultrafine Ti-6Al-4V sheet material, Metallurgical and Materials Transactions A: Physical Metallurgy and Materials Science 41 (2010) 499–512.

[6] A. Barnes, Superplastic forming 40 years and still growing, Journal of Materials Engineering and Performance 16 (2007) 440–454.

[7] E. Alabort, D. Barba, R. Reed, Mechanisms of Superplasticity in Titanium Alloys : Measurement , In Situ Observations and Rationalization, Defect and Diffusion Forum 385 (2018) 65–71.

[8] H. Masuda, H. Tobe, E. Sato, Y. Sugino, S. Ukai, Two-dimensional grain boundary sliding and mantle dislocation accommodation in ODS ferritic steel, Acta Materialia 120 (2016) 205–215.

[9] E. Sato, S. Ukai, H. Masuda, H. Tobe, Y. Sugino, Transgranular dislocation activities and substructural evolutions accommodating two-dimensional grain boundary sliding in ODS ferritic steel, Acta Materialia 132 (2017) 245–254.

[10] A. Geckinli, Grain boundary sliding model for superplastic deformation, Metal Science 17 (1983) 12–18.

[11] T. G. Langdon, Seventy-five years of superplasticity: historic developments and new opportunities, Journal of Materials Science 44 (2009) 5998–6010.

[12] S. Roy, S. Suwas, The influence of temperature and strain rate on the deformation response and microstructural evolution during hot compression of a titanium alloy Ti-6Al-4V-0.1B, Journal of Alloys and Compounds 548 (2013) 110–125.

[13] J. Kim, J. Kim, Y. Lee, C. Park, C. Lee, Microstructural analysis on boundary sliding and its accommodation mode during superplastic deformation of Ti-6Al-4V alloy, Materials Science and Engineering: A 263 (1999) 272–280.

[14] Q. Bai, J. Lin, T. Dean, D. Balint, T. Gao, Z. Zhang, Modelling of dominant softening mechanisms for Ti-6Al-4V in steady state hot forming conditions, Materials Science and Engineering: A 559 (2013) 352–358.

[15] X. Fan, H. Yang, Internal-state-variable based self-consistent constitutive modeling for hot working of two-phase titanium alloys coupling microstructure evolution, International Journal of Plasticity 27 (2011) 1833–1852.

[16] Q. Sun, G. Wang, M. Li, The superplasticity and microstructure evolution of TC11 titanium alloy, Materials & Design 32 (2011) 3893–3899.

[17] A. Momeni, S. Abbasi, Effect of hot working on flow behavior of Ti6Al4V alloy in single phase and two phase regions, Materials & Design 31 (2010) 3599–3604.

[18] S. L. Semiatin, M. W. Corbett, P. N. Fagin, G. A. Salishchev, C. S. Lee, Dynamic-Coarsening Behavior of an alpha /beta Titanium Alloy, Metallurgical and Materials Transactions A 37 (2006) 1125–1136.

[19] E. Alabort, P. Kontis, D. Barba, K. Dragnevski, R. C. Reed, On the mechanism of superplasticity in Ti 6Al 4V, Acta Materialia 105 (2016) 1–42.

[20] Y. G. Ko, C. S. Lee, D. H. Shin, S. L. Semiatin, Low-temperature superplasticity of ultra-fine-grained Ti-6Al-4V processed by equal-channel angular pressing, Metallurgical and Materials Transactions A 37 (2006) 381–391.

[21] S. V. Zherebtsov, E. A. Kudryavtsev, G. A. Salishchev, B. B. Straumal, S. L. Semiatin, Microstructure evolution and mechanical behavior of ultra-fine Ti[sbnd]6Al[sbnd]4V during low-temperature superplastic deformation, Acta Materialia 121 (2016) 152–163.

[22] R. Valiev, Nanostructuring of metals by severe plastic deformation for advanced properties., Nature materials 3 (2004) 511–516.

[23] J. R. Rumble (Ed.), Handbook of Chemistry and Physics, 2018.

[24] D. C. Leyens, D. M. Peters, Titanium and Titanium Alloys: Fundamentals and Applications, WileyVCH Verlag GmbH, 2005.

[25] G. Lutjering, J. C. Williams, Titanium, 2007.

[26] P. Li, D. H. Warner, A. Fatemi, N. Phan, Critical assessment of the fatigue performance of additively manufactured Ti-6Al-4V and perspective for future research, International Journal of Fatigue 85 (2016) 130–143.

[27] M. Zhou, Constitutive modeling of the viscoplastic deformation in high temperature forging of titanium alloy IMI834, Materials Science and Engineering: A 245 (1998) 29–38.

[28] Z. Sun, H. Yang, G. Han, X. Fan, A numerical model based on internal-state-variable method for the microstructure evolution during hot-working process of TA15 titanium alloy, Materials Science and Engineering: A 527 (2010) 3464–3471.

[29] F. Dunne, Inhomogeneity of microstructure in superplasticity and its effect on ductility, International Journal of Plasticity 14 (1998) 413–433.

[30] S. Semiatin, T. Bieler, The effect of alpha platelet thickness on plastic flow during hot working of Ti6Al4V with a transformed microstructure, Acta materialia 49 (2001) 3565–3573.

[31] J. Luo, M. Li, X. Li, Constitutive model for high temperature deformation of titanium alloys using internal state variables, Mechanics of Materials 42 (2010) 157–165.

[32] R. Picu, A. Majorell, Mechanical behavior of Ti-6Al-4V at high and moderate temperatures - Part II : constitutive modeling, Materials Science and Engineering: A 326 (2002) 306–316.

[33] J. H. Kim, S. Semiatin, C. S. Lee, Constitutive analysis of the high-temperature deformation of Ti6Al4V with a transformed microstructure, Acta Materialia 51 (2003) 5613–5626.

[34] M. Zhou, F. Dunne, Mechanisms-based constitutive equations for the superplastic behaviour of a titanium alloy, The Journal of Strain Analysis for Engineering Design 31 (2007) 187–196.

[35] J. Lin, Y. Liu, D. Farrugia, M. Zhou, Development of dislocation-based unified material model for simulating microstructure evolution in multipass hot rolling, Philosophical magazine 85 (2005) 1967–1987.

[36] J. Lin, Y. Liu, A set of unified constitutive equations for modelling microstructure evolution in hot deformation, Journal of materials processing technology 143-144 (2003) 281–285.

[37] E. Alabort, R. C. Reed, D. Barba, Combined modelling and miniaturised characterisation of high-temperature forging in a nickel-based superalloy, Materials and Design 160 (2018) 683–697.

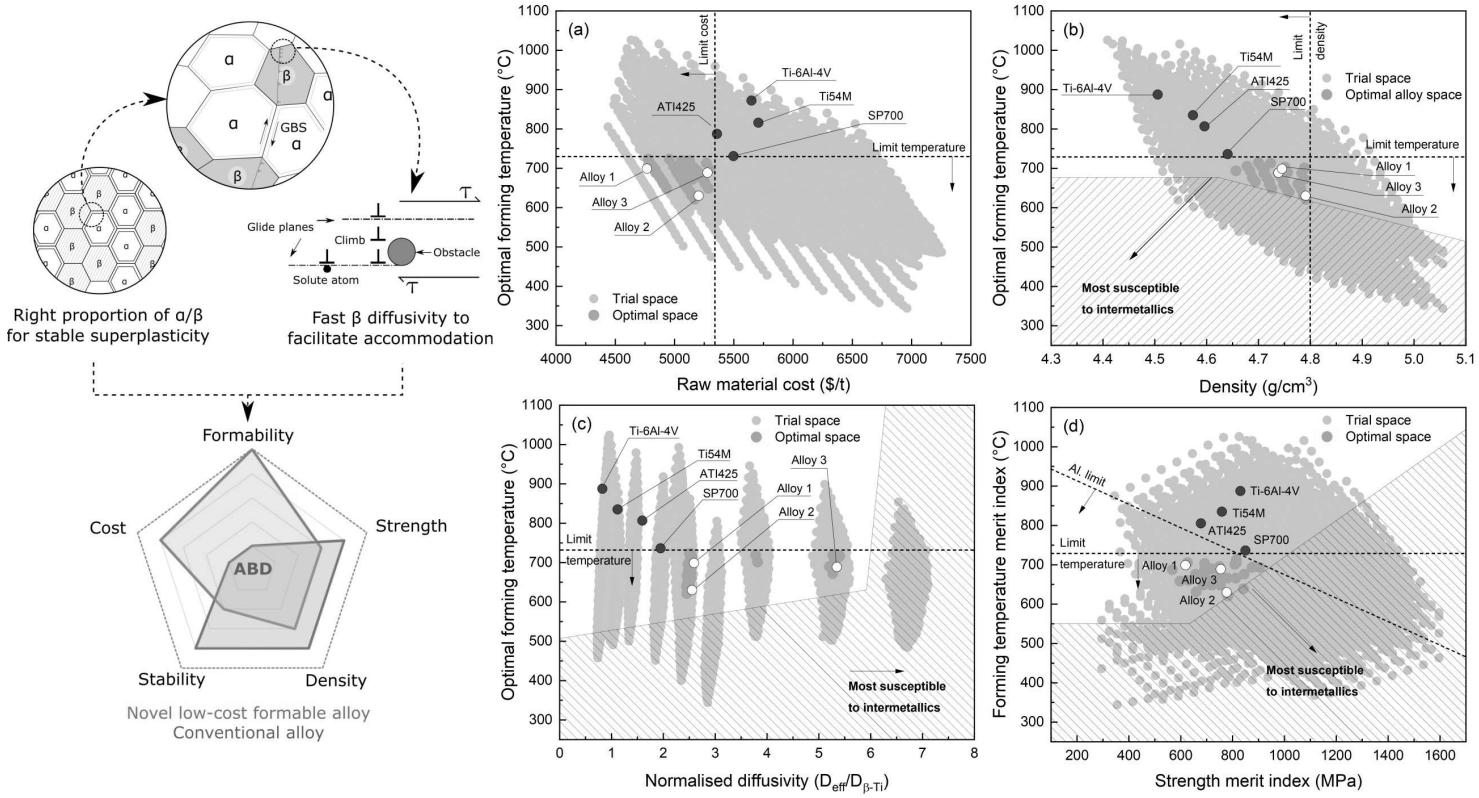

Figure 1: Left hand side shows the physical rationale behind the alloys-by-design (ABD) process together with property trade-off concept. Scatter plots compare trial composition space with baseline alloys against optimal alloy space and proposed examples for; (a) forming temperature vs. cost; (b) forming temperature vs. density; (c) forming temperature vs. diffusivity; and (d) forming temperature vs. strength.

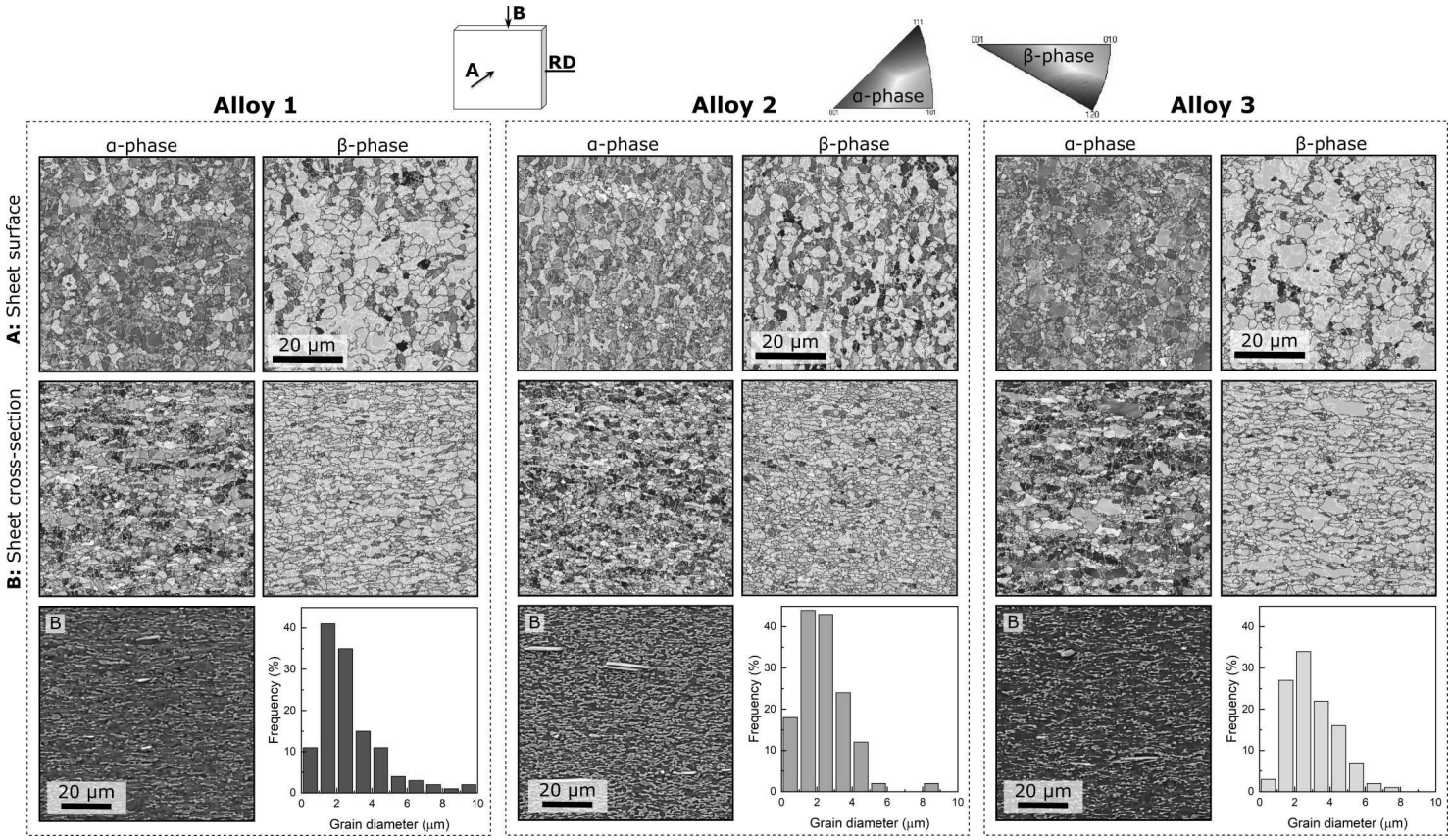

Figure 2: EBSD maps for α and β phases for each one of the designed alloys after processing together with SEM micrographs and frequency distributions of the grain size.

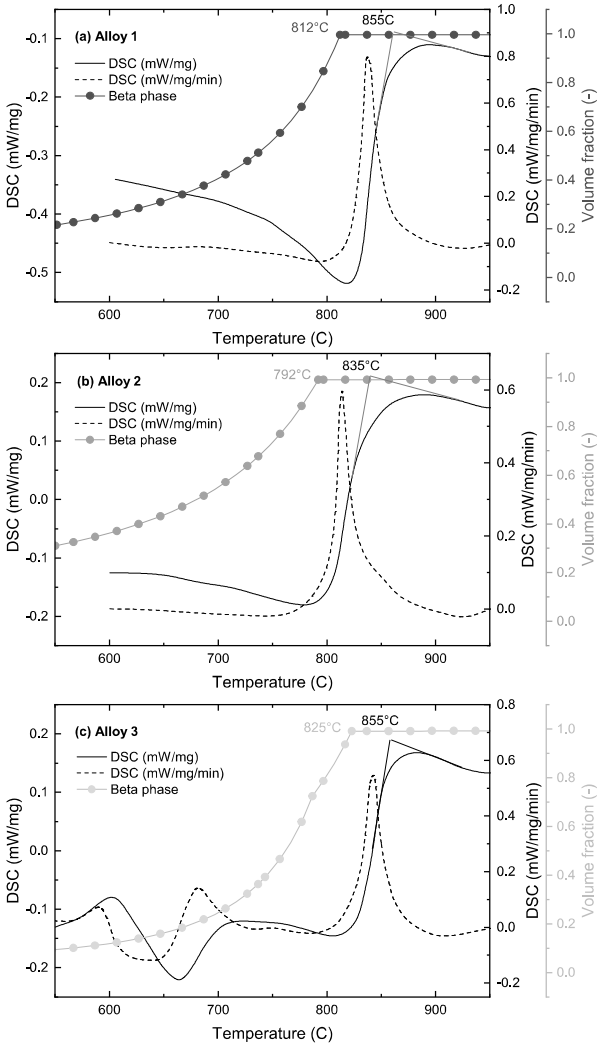

Figure 3: Experimental DSC data for each one of the designed alloys and comparison with the phase transformation of the β phase predicted by ThermoCalc.

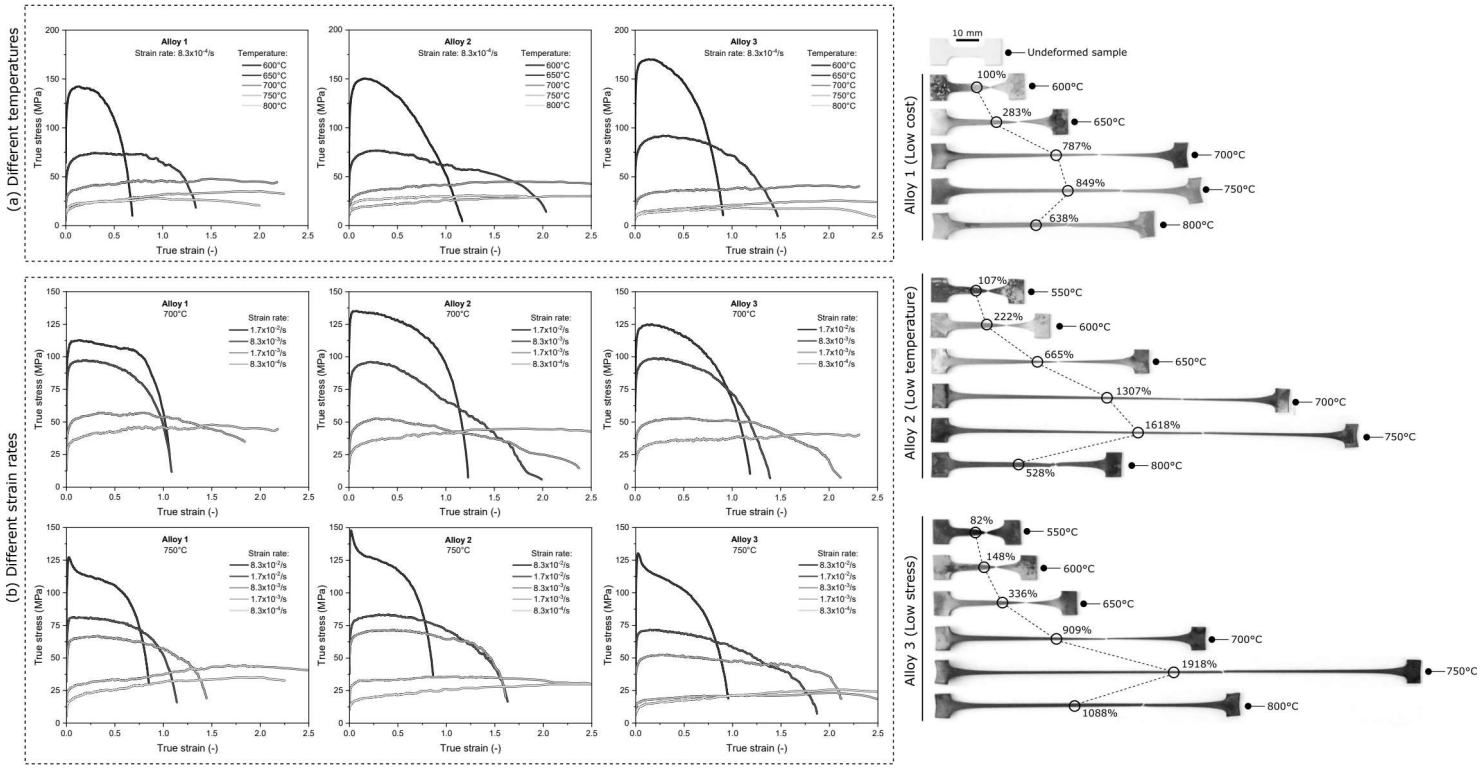

Figure 4: (a-b) Experimental stress - strain curves at temperatures between 600 and 800 °C for each one of the designed alloys.(Right) Images of the specimens after testing at a strain rate of 8.3×10^{-4}/s and different temperatures.

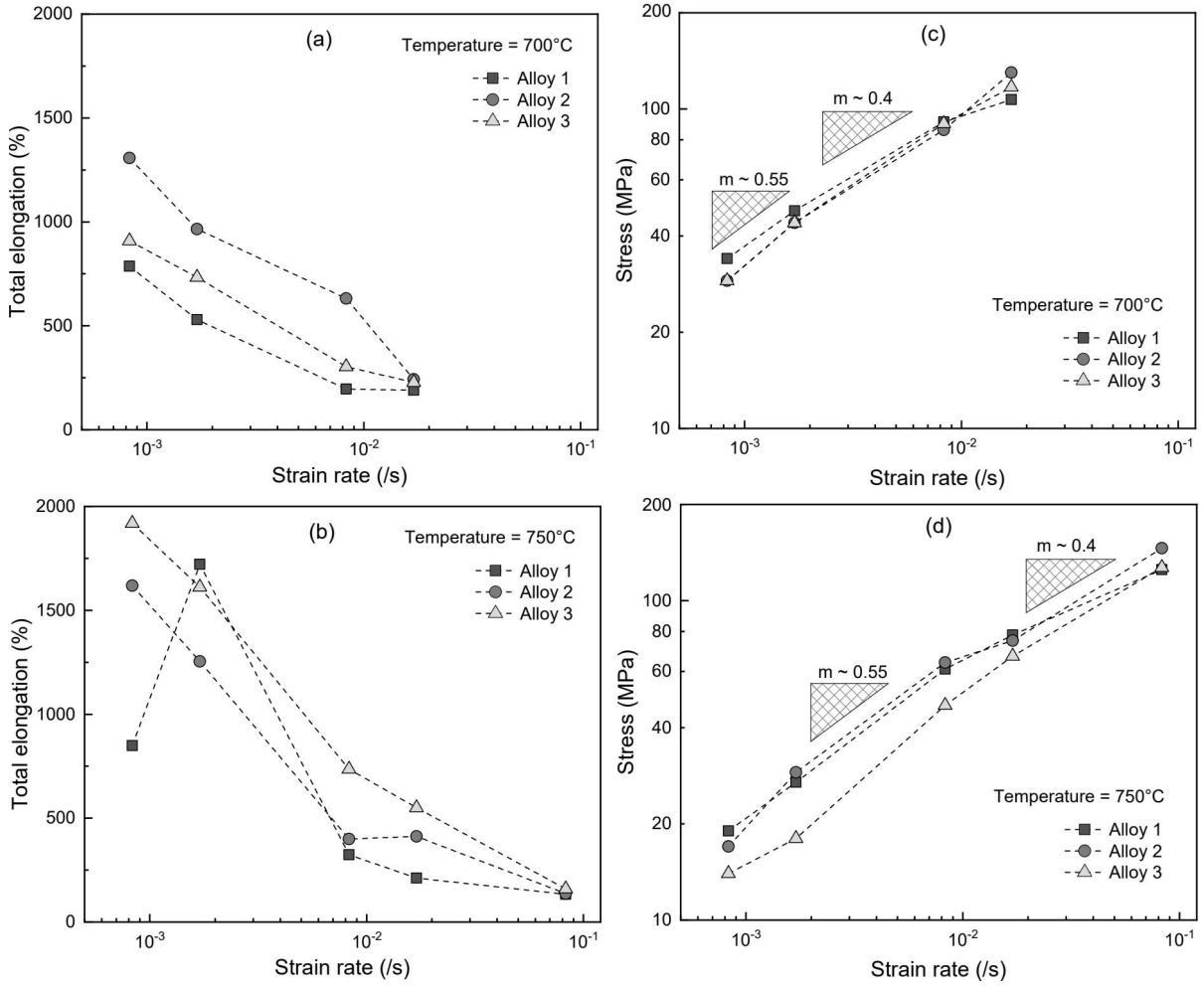

Figure 5: Total elongation as a function of the strain rate for the three alloys at: (a) 700, and (b) 750 °C. Experimental determination of the strain rate sensitivity parameter m as a function of strain rate at: (c) 700, and (d) 750 °C.

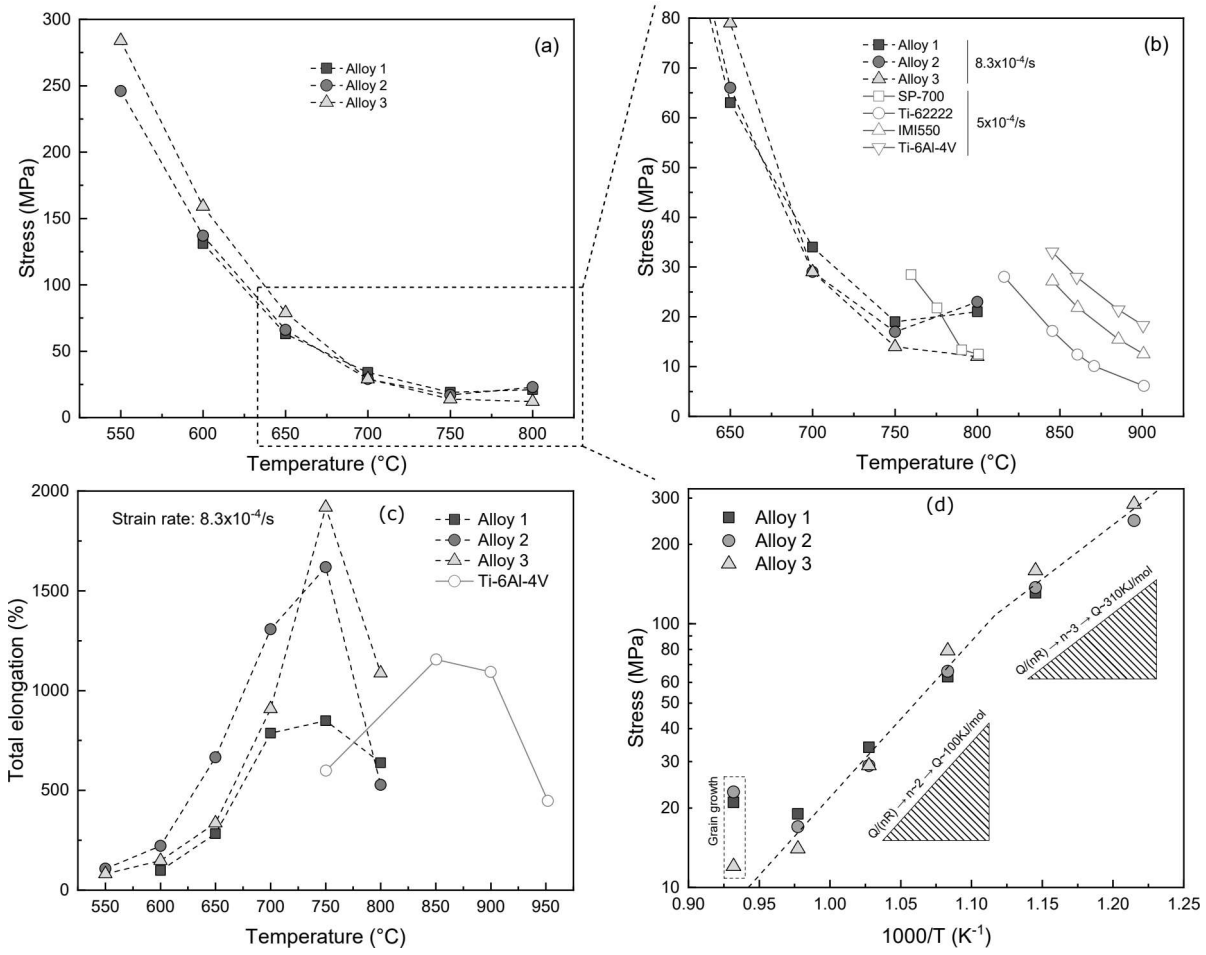

Figure 6: (a-b) Flow stress as a function of the testing temperature for the three designed alloys and comparison to the values of the baseline alloys provided in [25]. (c) Total elongation as a function of the temperature for the three designed alloys when deformed at 8.3×10^{-4}/s and comparison to values obtained with fine-grained Ti-6Al-4V [25].(d) Experimental determination of an apparent activation energy Q as a function of the inverse of the temperature for a strain rate of 8.3×10^{-4}/s.

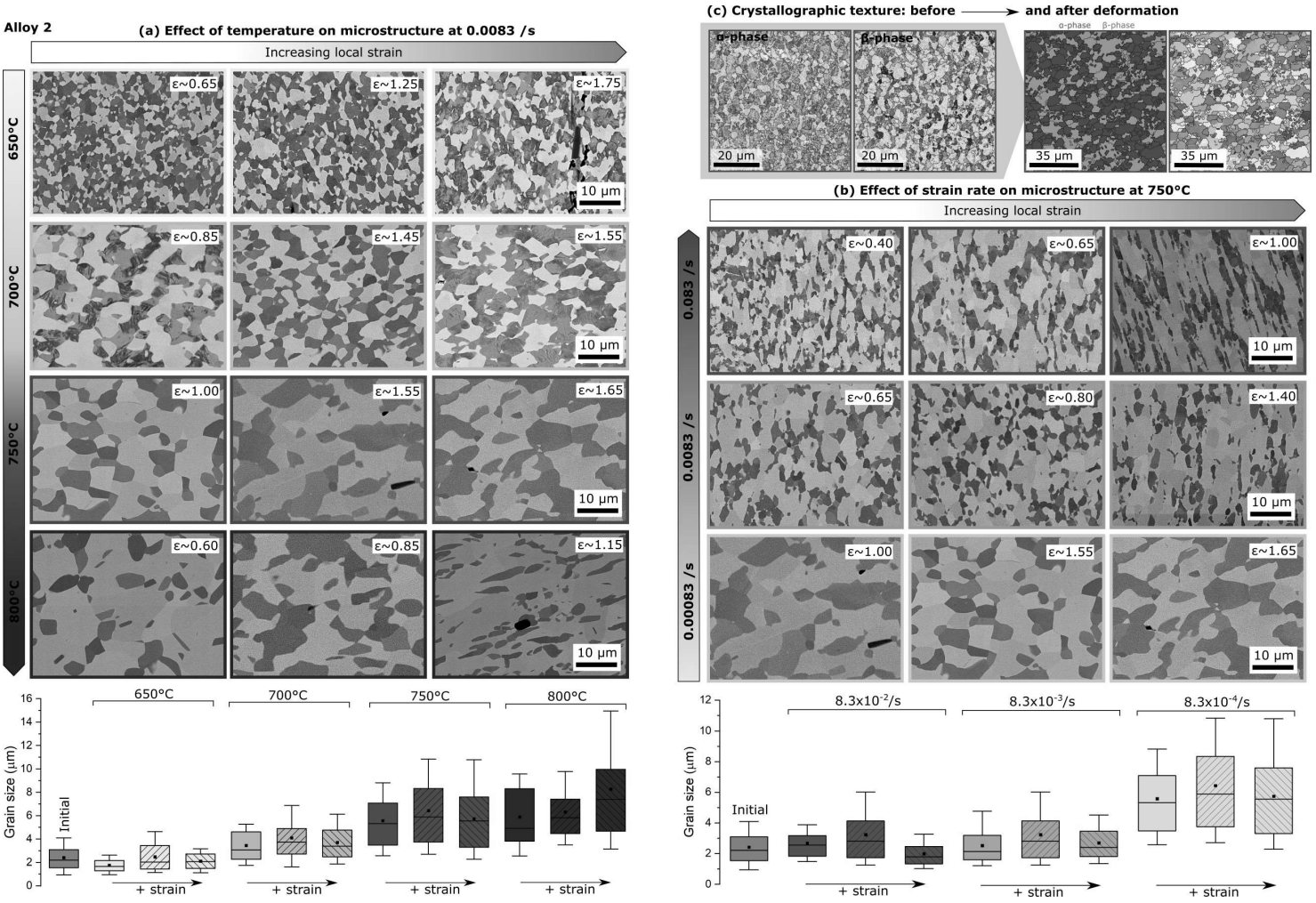

Figure 7: Micrographs of the microstructure of Alloy 2 after deformation at different temperatures, strain rates and strains (a-b). Also, EBSD scans of the microstructure before and after optimal superplastic deformation (c). The bar graphs at the bottom illustrate the mean grain size of both α and β phases as taken from the microgpahs: circles shows mean value, boxes indicate 25 and 75 percentile, box line shows the median, and whiskers shows the 10 and 90% values.

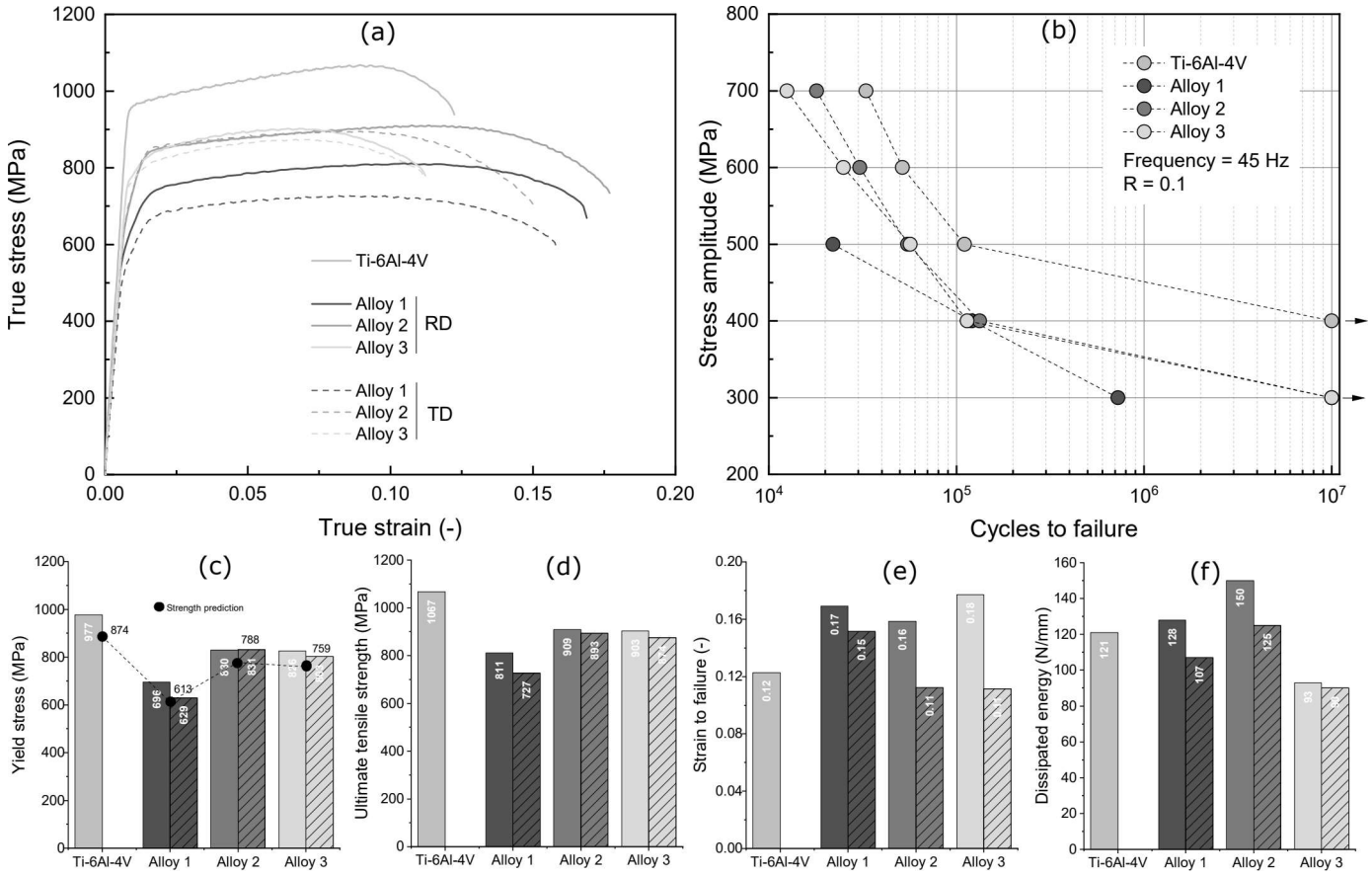

Figure 8: (a) True stress-true strain experimental values of the three designed alloys and the baseline Ti-6Al-4V. (b) Fatigue experimental values of the three designed alloys and the baseline Ti-6Al-4V. Summary of experimental values of: (c) the yield tensile strength, (d) the ultimate tensile strength, (e) the ductility, and (f) the dissipated energy of the three designed alloys when deformed at room temperature. Figure uses the fine-grained Ti-6Al-4V values as a baseline. Empty bars summarise results for the rolling direction while dashed bars summarise results for the transverse direction.

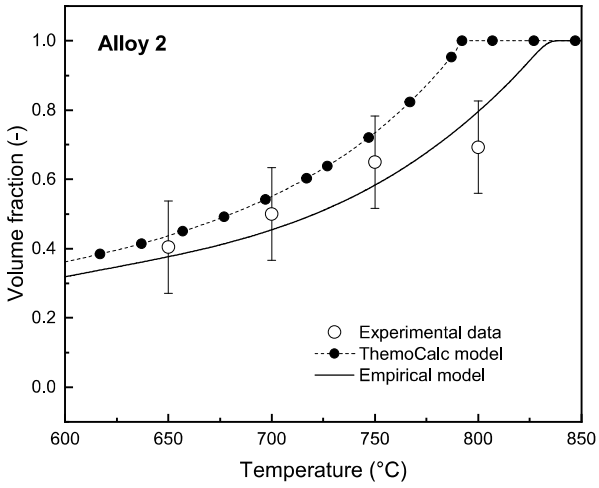

Figure 9: Experimental vs. computed curves for the volume fraction of β phase of Alloy 2 as a function of the temperature.

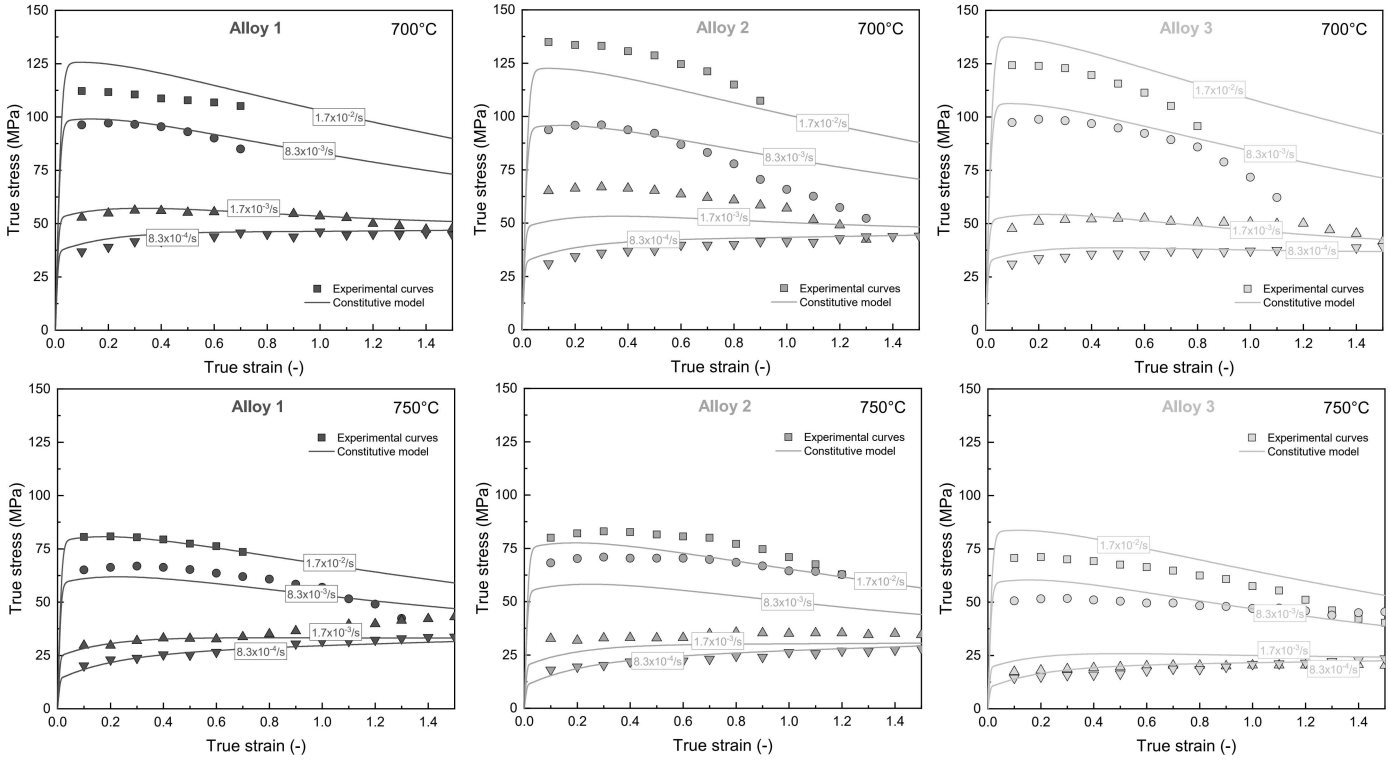

Figure 10: Experimental vs. computed true stress-true strain curves at 700 and 750 °C and different strain rates.

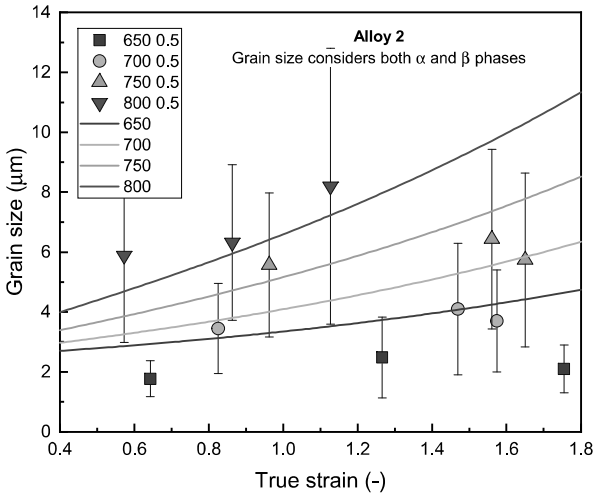

Figure 11: Experimental vs. computed mean grain size - true strain curves at 650, 700, 750 and 800 °C at a strain rate of 8.3×10^{-4}/s.

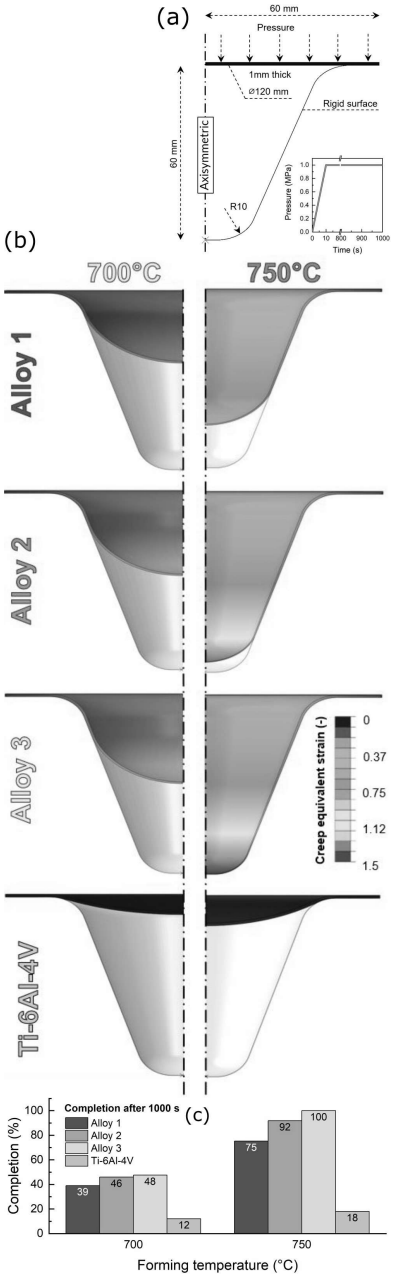

Figure 12: (a) Boundary and forming conditions together with geometrical description of the cone formability simulation. (b) Simulated distribution of creep equivalent strain at the end (1000 s of constant pressure) of the formability test for each one of the designed alloys at 700 (first column) and 750 °C (second column). (c) Percentage of completion of the formability test after 1000 seconds at constant pressure for the three alloys at 700 and 750 °C.